Int. J. Heat Mass Transfer. Vol. 32, No. 12, pp. 2409–2420, 1989
Printed in Great Britain

0017–9310/89 $3.00 + 0.00

Buoyancy and surface tension driven flows in float zone crystal growth with a strong axial magnetic field

K. H. LIE, D. N. RIAHI and J. S. WALKER

Department of Theoretical and Applied Mechanics, University of Illinois at Urbana-Champaign, 216 Talbot Laboratory, 104 South Wright Street, Urbana, IL 61801, U.S.A.

(*Received* 20 *October* 1988 *and in final form* 12 *March* 1989)

Abstract—The buoyancy driven flow due to the temperature gradient in the melt of a float zone and the surface tension driven flow due to the non-uniform temperature distribution along the free surface of the zone are studied in the presence of a strong axial magnetic field. The non-cylindrical shape of the zone is found to have a profound effect on the melt motion. The results indicate that the regions near the free surface are controlled mainly by the thermocapillarity, while the inner region is dominated by the buoyancy driven flow. Some implications for the mass transport of dopants in the molten float zone are discussed.

1. INTRODUCTION

IN THE float zone growth of a silicon crystal, the solid silicon of a feed rod is melted by a copper induction coil. Here we treat the coil as a wire loop, which is located at $z = 0$ and a radial distance of 7.6 mm away from the surface of the melt, and which carries an a.c. electric current, as shown in Fig. 1 [1]. We present results for one set of dimensions and physical constants which are typical of the float zone process, and we give these specific values in the Nomenclature. The free surface of the liquid silicon is stabilized by the electromagnetic body force from the coil. Figure 1 shows the lengthwise diagram of the float zone process with the induction coil and in the presence of a uniform, axial, d.c. magnetic field **B**. The actual positions of the crystal and feed rod faces relative to the induction coil are determined by the heat transfer in the melt, crystal and feed rod and by radiation between their surfaces and the surrounding surfaces. We only treat the heat transfer in the melt, so that we assume positions for the feed rod and crystal faces, namely at $z = \pm 1$. The experimental results presented by Robertson and O'Connor [2] indicate that the crystal–melt interface becomes nearly planar with a d.c. axial magnetic field of 0.5 T, so that we neglect any curvature of the crystal or feed rod face. The induction coil induces azimuthal electric currents near the surface of the liquid silicon. These electric currents are confined in a very thin free-surface layer called the skin depth [3]. Gupta *et al.* [4] showed that the thickness of this skin depth layer is about 0.29 mm for a radio frequency of 3 MHz in the induction coil. These surface electric currents generate the so-called Joulean heating which keeps the silicon molten and contributes to the temperature variation in the melt. This temperature variation in the melt can drive the thermal free-convective flow inside the melt and the Marangoni flow near the free-surface region.

The Boussinesq assumption is adopted here for constant physical parameters. The percentage error of the density (ρ) of the molten silicon due to the Boussinesq assumption is about 1.41E−03, the product of α and ΔT. Here we present asymptotic solutions for a strong axial d.c. magnetic field. For a silicon melt in the Czochralski process, Langlois *et al.* [5] compared the predictions of the strong-field asymptotic solutions with digital simulations of the full Navier–Stokes equations for $B = 0.2$ T. They found that the largest

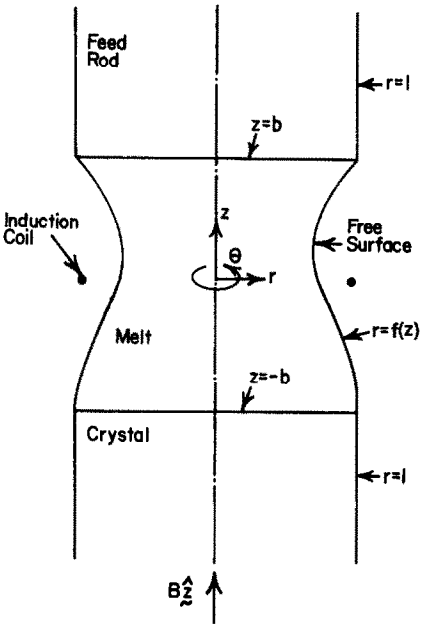

FIG. 1. Float zone process with induction heating by a single coil. (After Riahi and Walker [1].)

NOMENCLATURE

a horizontal distance between induction coil and melt surface, 7.6 mm
A_i, B_i, C_i, D_i coefficient matrices of order 19×19
B magnetic field strength [T]
C_h specific heat of molten silicon, 1.0E+03 J kg^{-1} K^{-1}
I peak electric current in the induction coil, 131.7 A
$\mathbf{j}$ electric current density vector [A m^{-2}]
k thermal conductivity of molten silicon, 46.6 W m^{-1} K^{-1}
M Hartmann number, $BR_c(\sigma/\rho\nu)^{1/2}$
(n, θ, t) curvilinear coordinates on free surface
N interaction number, $\sigma B^2 R_c/(\rho v_{ch})$ where $v_{ch} = v_b$ or v_{th}
p deviation of melt pressure from hydrostatic pressure
Pe Peclet number, $\rho C_h v_{ch} R_c/k$
(r, θ, z) cylindrical coordinates
R_c radius of the solid crystal, 0.0381 m
T temperature in the melt [K]
T_e effective temperature surrounding the melt [K]
T_s melting temperature of silicon, 1685 K
$T_i, \hat{E}, \hat{G}$ arrays of dimension 19
ΔT maximum temperature difference inside the molten silicon pool, 10 K
$\mathbf{v}$ velocity vector in the melt
v_b characteristic velocity for buoyancy flow, $\rho g \alpha \Delta T/(\sigma B^2)$
v_{ch} characteristic velocity: v_b for buoyancy flow; v_{th} for thermocapillary flow
v_{th} characteristic velocity for thermocapillary flow, $\Delta T|d\gamma/dT|/(\sigma B^2 R_c^2)$
(x, y) transformed coordinates from (r, z), $y = z$ and $x = r/f(z)$.

Greek symbols

α volumetric expansion coefficient of molten silicon, 1.41E−04 K^{-1}
γ surface tension of molten silicon, 0.736 N m^{-1}
δ skin depth on melt surface for 3.0 MHz a.c. current, 0.29 mm
ε_e effective emissivity of molten silicon, 0.26
ε_m electromagnetic Bond number, $\mu I^2/\gamma R_c$
κ thermal diffusivity of molten silicon, $k/\rho C_h$
λ angle between $\hat{n}$ and $\hat{z}$, $\cos^{-1}(\hat{n} \cdot \hat{z})$
μ magnetic permeability, 4πE−07 H m^{-1}
ν kinematic viscosity of molten silicon, 3.0E−07 m^2 s^{-1}
ξ stretched normal coordinate inside the free-surface Hartmann layer, Mn
ρ density of molten silicon at T_s, 2530 kg m^{-3}
σ electric conductivity of molten silicon, 1.0E+06 S m^{-1}
σ_r Stefan–Boltzmann constant for radiation, 5.67E−08 W m^{-2} K^{-4}
ϕ electric potential function inside the melt
ψ dimensionless stream function.

error in the asymptotic solution was the neglect of $O(M^{-1})$ terms. Here, $M = 1379B$, so that an $O(M^{-1})$ relative error for $B = 0.5$ T is comparable to the relative error in the Boussinesq approximation.

The dimensional form of the governing equations for the flow problem are composed of the conservation of mass and charge, Ohm's law, and the Navier–Stokes equations with the buoyancy and electromagnetic body forces included (see ref. [6]). These are

$$\rho(\mathbf{v} \cdot \nabla)\mathbf{v} = -\nabla p + \rho g \alpha (T - T_s)\mathbf{z} + \mathbf{j} \times \mathbf{B} + \rho \nu \nabla^2 \mathbf{v} \tag{1a}$$

$$\nabla \cdot \mathbf{v} = 0, \quad \mathbf{j} = \sigma(-\nabla \phi + \mathbf{v} \times \mathbf{B}) \tag{1b,c}$$

$$\nabla \cdot \mathbf{j} = 0, \quad \rho C_h \mathbf{v} \cdot \nabla T = k \nabla^2 T. \tag{1d,e}$$

The first-order perturbation term, $\alpha(T - T_s)$, for the density of the liquid silicon in the momentum equation is neglected due to the Boussinesq assumption. Because the flow is axisymmetric, only the meridional motion of the melt is investigated. The governing equations describing the meridional variables, v_r, v_z, j_θ, p, and T, are nondimensionalized using the characteristic length R_c for the space variables, the characteristic temperature difference ΔT for the temperature difference $(T - T_s)$ [7] and the characteristic velocity v_{ch} for the melt velocity. The selection of v_{ch} will be discussed later. The characteristic quantities $\sigma v_{ch} B$ and $\sigma v_{ch} B^2 R_c$ are used for j_θ and p, respectively. The resulting non-dimensional governing equations for the meridional variables are

$$N^{-1} D v_r = -\frac{\partial p}{\partial r} + j_\theta + M^{-2}\left(\nabla^2 v_r - \frac{v_r}{r^2}\right) \tag{2a}$$

$$N^{-1} D v_z = -\frac{\partial p}{\partial z} + v_{bc} T + M^{-2} \nabla^2 v_z \tag{2b}$$

$$\frac{\partial v_r}{\partial r} + \frac{v_r}{r} + \frac{\partial v_z}{\partial z} = 0 \tag{2c}$$

$$j_\theta = -v_r, \quad Pe\, DT = \nabla^2 T \qquad (2d,e)$$

where

$$D = v_r \frac{\partial}{\partial r} + v_z \frac{\partial}{\partial z}, \quad \nabla^2 = \frac{\partial^2}{\partial r^2} + \frac{1}{r}\frac{\partial}{\partial r} + \frac{\partial^2}{\partial z^2}.$$

Henceforth p, v_r, v_z, j_θ, and T are the dimensionless pressure, radial velocity, axial velocity, electric current density, and deviation of the temperature from T_s. Equation (2d) is the θ component of Ohm's law (1c) and does not involve ϕ because ϕ is independent of θ for an axisymmetric flow.

We assume that N is sufficiently large that the inertial terms on the left-hand side of equations (2a) and (2b) can be neglected. Since the inertialess momentum equation is linear, we can treat several components of the melt motion independently and then superpose these components. The independent components of the melt motion are the forced convection due to centrifugal pumping if the crystal or feed rod are rotating about the z-axis, the free convection due to buoyancy, the Marangoni or thermocapillary convection due to the temperature-dependent surface tension, the forced convection due to the a.c. electromagnetic body force in the skin depth layer, and the motion from the melting feed rod face to the crystal face. Here we consider only the buoyant and thermocapillary convections which are thermally driven and which are independent of the other components for $N \gg 1$.

The buoyant and thermocapillary convections involve radial and axial velocities for axisymmetric temperatures and only induce azimuthal electric current densities j_θ. The electric potential ϕ and the other components of the electric current density j_r and j_z are governed by a homogeneous boundary value problem, and these variables are zero [8]. For the flow associated with the crystal and feed rod rotations, there is an azimuthal velocity v_θ and non-zero values of ϕ, j_r, and j_z [6]. These flows are decoupled because of the strong magnetic field approximation. We note that **j** here is the d.c. electric current density induced by the steady-state thermal convection across the d.c. applied magnetic field **B**. The radio-frequency a.c. magnetic field and current density are confined to a skin-depth layer at the free surface and only enter the present problem as a heat source at the free surface due to the Joulean heating in the a.c. current.

For $M \gg 1$, the viscous terms in equations (2a) and (2b) can be neglected except in thin boundary and interior layers. The subregions of the melt for a uniform, axial d.c. magnetic field are shown in Fig. 2. The regions i, u, and l are the inner, upper, and lower cores where the viscous terms can be neglected. The viscous Hartmann layers h adjacent to the free surface, crystal and feed rod have an $O(M^{-1})$ dimensionless thickness because there is a non-zero component of the d.c. magnetic field perpendicular to each surface. The interior or free shear layer f lies along the d.c. magnetic field line tangent to the neck of the melt,

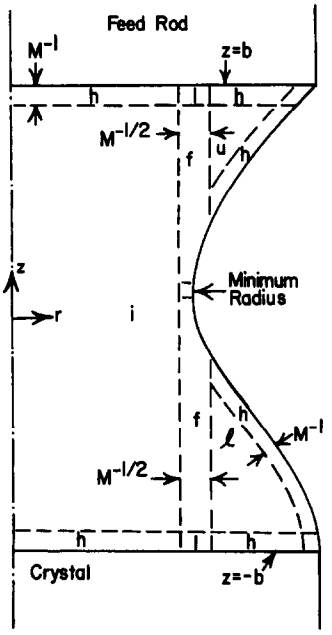

FIG. 2. Subregions in the melt (h, Hartmann layer; I, interaction region; f, free shear layer; i, inner core region; u, upper outer core region; l, lower outer core region).

has an $O(M^{-1/2})$ dimensionless thickness because the layer is parallel to the magnetic field and matches jumps between the inner core i and the outer cores u and l [9].

The solutions for the buoyant and thermocapillary convections are presented in Sections 2 and 3, respectively. We have assumed that N is sufficiently large to neglect inertial effects, which permits independent solutions for several components of the melt motion. However, the value of N depends on the characteristic velocity v_{ch} which has not yet been defined. The balance between the d.c. electromagnetic body force opposing the melt motion and either the buoyant or thermocapillary driving force provides a definition of v_{ch}, either v_b or v_{th}. If the N based on both values is sufficiently large, our inertialess assumption is valid.

Langlois *et al.* [5] present digital simulations of the Navier–Stokes equations for the melt motion in a Czochralski crystal puller with a uniform, axial, d.c. magnetic field. For $B = 0.2$ T, they artificially increase the value of N by a factor of four with all other parameters fixed in order to estimate the role of inertial effects. This change has a negligible effect on the results, indicating that inertial effects are indeed negligible. Their value of $B = 0.2$ T corresponds to approximately 600 for the N discussed in the next two sections. The strong-field asymptotic solutions complement the digital simulations of the Navier–Stokes equations in two ways. First, the digital simulation becomes more difficult as B is increased because grids must become more refined to resolve boundary layers, while the asymptotic solutions improve as B is increased. Second, the asymptotic solutions are quite

simple and permit the practical investigation of a large number of crystal growth conditions. Once promising conditions are identified, digital simulations for a few cases can provide more accuracy.

2. BUOYANCY DRIVEN FLOW

For the buoyancy driven flow, the motion of liquid silicon is caused by the free convection due to the temperature variation within the liquid silicon. For the temperature field, there is no free shear layer to divide the core region in the melt into different core temperature regions (see ref. [8]). Therefore, the entire molten zone is treated as a single domain for temperature. Because a strong axial magnetic field is considered, the momentum equation for velocity and the heat equation for temperature are decoupled by ignoring the convection term in the heat equation. For the buoyancy driven motion we choose

$$v_{ch} = v_b = \rho g \alpha \Delta T/(\sigma B^2)$$

so that $v_{bc} = 1$, while

$$N = \sigma^2 B^4 R_c/(\rho^2 g \alpha \Delta T), \quad Pe = \rho g \alpha \Delta T R_c/(\sigma B^2 \kappa).$$

The values of v_b, Pe, and N are listed in Table 1 for several values of axial magnetic field strength B.

The values of N in Table 1 are above 600 for $B \geqslant 0.2$ T, so that the inertialess assumption is valid. Hjellming and Walker [10, 11] solved for the temperature in a Czochralski crystal puller with an axial magnetic field. Their results indicate that convective heat transport is negligible for $Pe < 1.0$, with Pe defined with the same $v_{ch} = v_b$. We neglect the convective heat transport term on the left-hand side of equation (2e) so that this equation is also linear. The values of Pe in Table 1 indicate that the present analysis should be valid for $B \geqslant 0.3$ T.

After neglecting convection terms in the heat equation, the temperature field is governed by a Laplace equation with the boundary conditions based on Joulean heating, the Stefan–Boltzmann radiation equation applied to the free surface and the temperatures at the crystal and feed rod interfaces [11]. The Joulean heating term due to the a.c. electric current in the free surface skin-depth layer is $I^2a^2/((a^2+z^2)^2 \times \sqrt{8k\sigma\delta\pi^2 R_c^3})$, where a and δ are normalized by R_c. This coil current I corresponds to an electromagnetic Bond number of 0.8 and we use the free-surface shape corresponding to this electromagnetic Bond number [1]. Following ref. [11], the radiation equation at the free surface is written as

$$\frac{\partial T}{\partial n} = -C_0 - C_1 T, \text{ on the free surface}$$

with

$$C_0 = \varepsilon_e \sigma_r R_c (T_s^4 - T_e^4)/k\Delta T \quad \text{and} \quad C_1 = 4R_c \varepsilon_e \sigma_r T_s^3/k$$

while T_e is determined later. The dimensional variables for the radial variable r (or the axial variable z) and for the temperature $(T - T_s)$ in the heat equation can be nondimensionalized by R_c and ΔT, respectively. Therefore, the boundary values for the dimensionless temperature along the melting and solidifying interfaces are zero. We thus obtain the following dimensionless governing equation and the boundary conditions for the liquid silicon temperature:

$$\nabla^2 T = 0, \text{ in the melt} \tag{3a}$$

$$T = 0, \quad \text{at} \quad z = \pm 1 \tag{3b}$$

$$\frac{\partial T}{\partial r} = 0, \quad \text{as} \quad r = 0 \tag{3c}$$

and

$$\underset{\sim}{\hat{n}} \cdot \underset{\sim}{\nabla} T = A/(a^2+z^2)^2 - C_0 - C_1 T, \quad \text{at} \quad r = f(z) \tag{3d}$$

where

$$\nabla^2 = \frac{\partial^2}{\partial r^2} + \frac{\partial}{r\partial r} + \frac{\partial^2}{\partial z^2}$$

$\underset{\sim}{\hat{n}}$ is a unit normal vector to the free surface at $r = f(z)$ and $A = I^2a^2/(\sqrt{8k\sigma\delta\pi^2 R_c^3 \Delta T})$. Due to the non-cylindrical shape of the free surface, non-orthogonal coordinates are adopted in order to transform the hour-glass shape into a straight cylindrical domain [12]. The original r, z coordinates are transformed into x, y coordinates by

$$y = z \quad \text{and} \quad x = r/f(z).$$

The control-volume approach is applied here to the new transformed heat equation in order to obtain the corresponding finite difference equation:

$$\int_{\mathscr{V}} \nabla^2 T \, d\mathscr{V} = \int_{\mathscr{A}} \underset{\sim}{n} \cdot \underset{\sim}{\nabla} Tr \, dS \, d\theta = 0$$

where $\underset{\sim}{n}$ is the unit vector normal to the surface of the

Table 1. The magnitudes of v_b, Pe, and N of the buoyancy driven flow corresponding to various axial magnetic field strengths B

B(T)	v_b (m s^{-1})	Pe	N
0.1	0.349952E−02	0.721983E+01	0.429195E+02
0.2	0.874880E−03	0.180496E+01	0.686712E+03
0.3	0.388836E−03	0.802203E+00	0.347648E+04
0.4	0.218720E−03	0.451239E+00	0.109874E+05
0.5	0.139981E−03	0.288793E+00	0.268247E+05
0.6	0.972089E−04	0.200551E+00	0.556236E+05
0.7	0.714188E−04	0.147343E+00	0.103050E+06
0.8	0.546800E−04	0.112810E+00	0.175798E+06
0.9	0.432040E−04	0.891337E−01	0.281595E+06
1.0	0.349952E−04	0.721983E−01	0.429195E+06

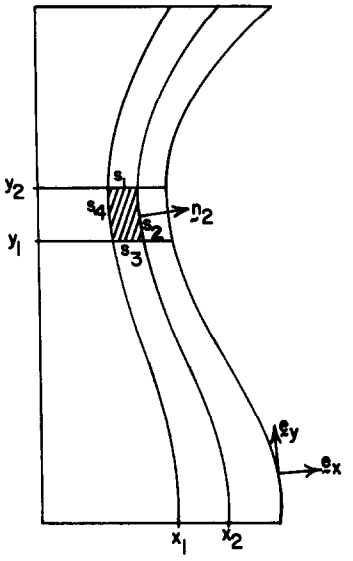

FIG. 3. The control surface cell for the finite difference grid in the glass shaped melt.

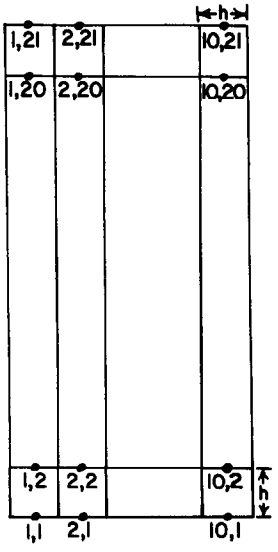

FIG. 4. The 10×21 finite difference grid for the transformed cylindrical domain, with $\Delta x = \Delta y = h$.

control volume (see Fig. 3). The surface integral can be treated as a line integral over contours, S_1, S_2, S_3, and S_4, shown in Fig. 3, by integrating over a wedge portion of the cylinder for a constant azimuthal angle θ because of the property of axisymmetry. Therefore

$$\int_S \underset{\sim}{n} \cdot \underset{\sim}{\nabla} Tr \, dS = 0 \tag{4}$$

and the expressions for $\underset{\sim}{n} \cdot \underset{\sim}{\nabla}$ and dS for each surface over the control area are derived as

$$\underset{\sim}{n}_1 \cdot \underset{\sim}{\nabla} = \frac{\partial}{\partial y} - \frac{xf'(x)}{f(x)} \frac{\partial}{\partial x} \quad \text{and} \quad dS_1 = f(y)\, dx, \quad \text{for} \quad S_1$$

$$\underset{\sim}{n}_2 \cdot \underset{\sim}{\nabla} = \frac{\alpha(x,y)}{f(y)} \frac{\partial}{\partial x} - \frac{xf'(y)}{\alpha(x,y)} \frac{\partial}{\partial y} \quad \text{and} \quad dS_2 = \sqrt{(\alpha(x,y))}\, dy, \quad \text{for} \quad S_2$$

$$\underset{\sim}{n}_3 \cdot \underset{\sim}{\nabla} = -\underset{\sim}{n}_1 \cdot \underset{\sim}{\nabla} \quad \text{and} \quad dS_3 = dS_1, \quad \text{for} \quad S_3$$

$$\underset{\sim}{n}_4 \cdot \underset{\sim}{\nabla} = -\underset{\sim}{n}_2 \cdot \underset{\sim}{\nabla} \quad \text{and} \quad dS_4 = dS_2, \quad \text{for} \quad S_4$$

where $\alpha(x, y) = 1 + (xf'(y))^2$. A polynomial approximation for free-surface shape $f(y)$ is obtained by a least squares curve fitting scheme using the free-surface shape associated with an electromagnetic Bond number ε_m of 0.8, $a = 7.6$ mm and $b = R_c$ [1]. With fourth-order polynomials, the relative errors between $f(y)$ and the original data are less than 1%

$$f(y) = 0.5926 - 0.3953y + 0.5175y^2 + 0.4003y^3 - 0.1267y^4.$$

The finite difference formula for the temperature is obtained by substituting $\underset{\sim}{n} \cdot \underset{\sim}{\nabla}$ and dS into equation (4). The resulting lengthy difference equation for temperature is not listed here. The boundary conditions along the interfaces between the solid and liquid silicon as well as the condition at $x = 0$ are not changed by the transformation, while the r-directional temperature gradient at the free surface of the untransformed shape is changed quite significantly. The transformed dimensionless boundary conditions are

$$T = 0, \quad \text{at} \quad y = \pm 1 \tag{5a}$$

$$x\partial T/\partial x \to 0, \quad \text{as} \quad x \to 0 \tag{5b}$$

$$\partial T/\partial x = f(y)[f'(y)\partial T/\partial y + \sqrt{(\alpha(x,y))}(A/(a^2+y^2)^2 - C_0 - C_1 T)]/\alpha(x,y), \quad \text{at} \quad x = 1. \tag{5c}$$

A 10×21 mesh is set up in the transformed cylindrical domain as shown in Fig. 4. An algebraic system of equations for the unknown matrices is derived from the resulting difference equation and boundary conditions (5) for temperature. This algebraic system of equations is further constructed to the following matrix equation:

$$\begin{vmatrix} B_1 & C_1 & & & & \\ A_2 & B_2 & C_2 & & & \\ & & & 0 & & \\ & \cdots & & & & \\ & & \cdots & & & \\ 0 & & A_9 & B_9 & C_9 & \\ & & & & A_{10} & B_{10} \end{vmatrix} \times \begin{vmatrix} \hat{T}_1 \\ \hat{T}_2 \\ \\ \vdots \\ \\ \hat{T}_9 \\ \hat{T}_{10} \end{vmatrix} = \begin{vmatrix} \\ \\ \\ 0 \\ \\ \\ \hat{E} \end{vmatrix} \tag{6}$$

where A_i, B_i and C_i are coefficient matrices of order 19×19, $\hat{T}_i$ represents the unknown temperature arrays of dimension 19 at the ith column, and $\hat{E}$ is an array generated by the heating and radiating boundary condition at the free surface. The general Gauss elimination method is applied to equation (6). First, the forward sweep is used for constructing an upper triangular matrix the elements of which consist of

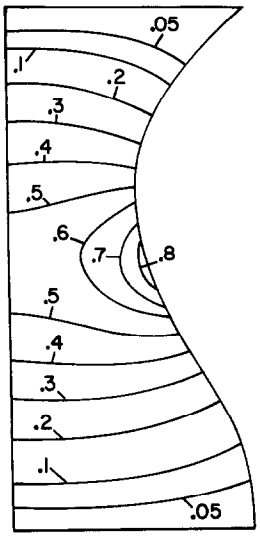

FIG. 5. The isotherms in the melt for $\varepsilon_m = 0.8$ and $T_e = 1680$ K.

unitary values on the diagonal line and matrices D_i located on the site of matrix C_i, $D_1 = B_1^{-1} \cdot C_1$ and $D_i = (-A_i \cdot D_{i-1} + B_i)^{-1} \cdot C_i$ with $i = 2, \ldots, 9$, and the new array $\hat{G} = (B_{10} - A_{10} \cdot D_9)^{-1} \cdot \hat{E}$ replaces the array $\hat{E}$ after the forward sweep step. Second, the backward sweep is used to derive the recurrence formula for temperature vectors $\hat{T}_i$

$$\hat{T}_{10} = \hat{G} \quad \text{and} \quad \hat{T}_i = -D_i \hat{T}_{i+1}, \quad i = 1, \ldots, 9.$$

The isotherms for the temperature field in the melt are plotted in Fig. 5 in the original (r, z) coordinates with an effective background temperature $T_e = 1680$ K, and the maximum dimensionless temperature (0.86) in the melt occurs at $(r, z) = (0.563, 0.00)$ which is the closest grid point to the free surface, about a normal distance of 0.83 mm away from the free surface. We presume that the temperature at the hottest surface spot would be very close to the expected 10 K above the melting temperature. Therefore, the temperature distribution for the specific dimensions and constants considered here is used for our next computation of the velocity field in the melt, because it gives an approximately accurate temperature difference ΔT inside the melt.

To investigate the melt motion due to buoyancy, the $O(1)$ pressure gradient, the velocities and the electric current density terms are included in the momentum equation with the temperature distribution provided from the above calculation. The dimensionless governing equations for the meridional melt motion in the inviscid cores (regions away from the boundaries), with only the $O(1)$ terms considered, are

$$\frac{\partial p}{\partial r} = -v_r \tag{7a}$$

$$\frac{\partial p}{\partial z} = T \tag{7b}$$

$$\frac{\partial v_r}{\partial r} + \frac{v_r}{r} + \frac{\partial v_z}{\partial z} = 0 \tag{7c}$$

while the boundary conditions for the velocity are

$$v_r = f' v_z, \quad \text{at} \quad r = f(z)$$

and

$$v_z = 0, \quad \text{at} \quad z = \pm 1.$$

The Hartmann layers at the free surface or at a solid–liquid interface match any tangential core velocity and satisfy the no-traction or no-slip condition provided that the normal component of the core velocity is zero.

The subregions for the velocity variable in this hour-glass shaped melt need to be considered separately. We introduce the stream function for the core velocities

$$v_r = -j_\theta = \frac{\partial \psi}{r \partial z}, \quad v_z = -\frac{\partial \psi}{r \partial r}$$

and we add the subscripts i, u, and l to denote the inner, upper, and lower core regions, respectively. Substituting these stream function identities for velocities in equations (7), the dimensionless solutions for ψ in different core regions are obtained

$$\psi_i(r, z) = \frac{r(z+1)}{2} \int_{-1}^{1} (1 - \varkappa) \frac{\partial T_i}{\partial r}(r, \varkappa)\, d\varkappa - r \int_{-1}^{z} (z - \varkappa) \frac{\partial T_i}{\partial r}(r, \varkappa)\, d\varkappa \tag{8a}$$

$$\psi_u(r, z) = \frac{r(1-z)}{1 - g_1(r)} \int_{g_1(r)}^{1} (\varkappa - g_1(r)) \frac{\partial T_u}{\partial r}(r, \varkappa)\, d\varkappa - r \int_{z}^{1} (\varkappa - z) \frac{\partial T_u}{\partial r}(r, \varkappa)\, d\varkappa \tag{8b}$$

$$\psi_l(r, z) = \frac{r(1+z)}{1 + g_2(r)} \int_{-1}^{g_2(r)} (g_2(r) - \varkappa) \frac{\partial T_l}{\partial r}(r, \varkappa)\, d\varkappa - r \int_{-1}^{z} (z - \varkappa) \frac{\partial T_l}{\partial r}(r, \varkappa)\, d\varkappa \tag{8c}$$

where $z = g_1(r)$ and $z = g_2(r)$ are the locations of the free surface above and below the point of minimum radius (see Fig. 6), i.e. the inverse of $r = f(z)$.

The streamlines based on equations (8) are calculated and plotted in Fig. 7. The melt motion basically flows upward in hot areas and downward in cold areas in all the regions. The upper outer core region involves a clockwise circulation, which is driven by negative temperature gradients, $\partial T/\partial r < 0$, in the r-direction in this region. We note that a strong positive temperature gradient, $\partial T/\partial r > 0$, exists near the upper corner of the lower outer core region, leading to the existence of a small counterclockwise circulation above the main clockwise circulation in the lower region. The free shear layer, which separates the outer and inner regions, provides space for developing an

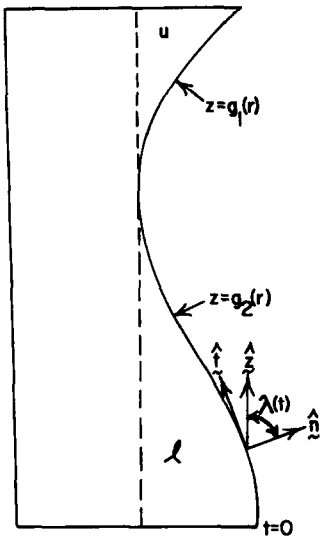

FIG. 6. The locations for the upper surface function $g_1(r)$ and the lower surface function $g_2(r)$.

up-flowing jet through the entire height of the liquid silicon. The motion in the inner core region has the strongest circulation among all the three regions, while the upper outer core region possesses the weakest circulation. The buoyancy driven circulation in an axial magnetic field varies roughly as the square of the vertical dimension of a region. The inner core region has the largest unobstructed vertical dimension while the upper outer core region has the smallest.

In case of large Peclet number, the convective heat transport term needs to be included in solving for the temperature field as the axial magnetic field strength is reduced. The temperature distribution with heat transport included is expected to be similar to Fig. 5, except that hot fluid will be lifted toward the top

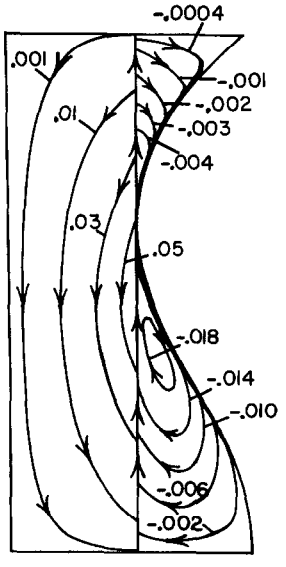

FIG. 7. The streamlines, nondimensionalized by v_b, due to buoyancy in the melt for $\varepsilon_m = 0.8$ and $T_e \simeq 1680$ K.

Table 2. The magnitudes of v_{th}, Pe, and N of the thermocapillary flow corresponding to various axial magnetic field strengths, B

B(T)	v_{th} (m s^{-1})	Pe	N
0.1	0.193213E−03	0.398616E+00	0.777367E+03
0.2	0.483033E−04	0.996541E−01	0.124379E+05
0.3	0.214681E−04	0.442907E−01	0.629667E+05
0.4	0.120758E−04	0.249135E−01	0.199006E+06
0.5	0.772853E−05	0.159447E−01	0.485854E+06
0.6	0.536704E−05	0.110727E−01	0.100747E+07
0.7	0.394313E−05	0.813503E−02	0.186646E+07
0.8	0.301896E−05	0.622838E−02	0.318409E+07
0.9	0.238535E−05	0.492119E−02	0.510030E+07
1.0	0.193213E−05	0.398616E−02	0.777367E+07

interface and subsequently the magnitudes of the radial temperature gradient will be smaller. The resulting circulations of the melt will then be slightly lifted, but the direction of the circulation will not be reversed.

3. SURFACE TENSION DRIVEN FLOW

With the temperature distribution discussed in the previous section, the surface tension driven flow due to the non-uniform free-surface temperature distribution is studied. The flow field of the melt is again divided into several regions, for $M \gg 1$, while our main concern is the free-surface Hartmann layer and the outer core regions, which are the regions affected by the forces due to the surface tension of the free surface. Unlike the case of the centrifugally driven motion [8], the surface traction is not zero in the free-surface Hartmann layer. The tangential surface tension gradient balances the viscous shear stress at the free surface which gives the characteristic velocity for the Marangoni flow. Therefore, v_{ch} is derived from the ratio of the shear stress due to thermocapillarity at the free surface to the electromagnetic resistance force inside the free-surface Hartmann layers and is defined as

$$v_{ch} = v_{th} = \Delta T|d\gamma/dT|/(\sigma B^2 R_c^2).$$

With $d\gamma/dT = -0.279E-03$ (N m^{-1} K^{-1}) [8], the buoyancy parameter v_{bc} is estimated as

$$v_{bc} = v_b/v_{th} = \rho g \alpha R_c^2/|d\gamma/dT| = 18.1122$$

which is the multiplication factor for dimensionless buoyancy driven velocity when it is combined with the thermocapillary velocity to give the thermal convective velocity in the melt.

Table 2 gives the magnitudes of the characteristic velocity v_{th}, the Peclet number $Pe = v_{th}R_c/\kappa$ and the interaction parameter $N = \sigma B^2 R_c/(\rho v_{th})$ for the thermocapillary motion for various axial magnetic field strengths, B.

From Table 2, we see that both the convective heat transport and the inertial effects in the Marangoni convection are not very significant because of the mag-

nitudes of the Peclet number and the interaction parameter. The governing equations in the different regions are derived from equations (1): the momentum equation without the inertial and buoyancy terms, the conservation of mass and charge and Ohm's law. Since the electromagnetic resistive force is very strong, the primary flow driven by the surface tension variation is confined to the Hartmann layer at the free surface. These free-surface jets from hot points to cold points complete their circulation through the upper and lower outer core regions. From the conservation of mass, the net flux, driven by the thermocapillarity, across any constant r-plane in the melt through the core region and the free-surface Hartmann layer is zero.

First, we start with the free-surface Hartmann layer. We define (n, θ, t) to be an orthogonal curvilinear coordinate system for normal, azimuthal and tangential variables on the free surface and $\lambda(t)$ to be the angle between the unit axial vector $\hat{z}$ of the cylindrical coordinates and the unit normal vector $\hat{n}$ at each point on the free surface. The governing equations are transformed from cylindrical coordinates (r, θ, z) into (n, θ, t) coordinates with

$$\hat{n} = (-g_2'/\sqrt{(1+g_2'^2)})\hat{r} + (1/\sqrt{(1+g_2'^2)})\hat{z}$$

calculated from the lower surface expression $z = g_2(r)$. The normal coordinate n of the resulting equations, which are not written here, is stretched by introducing $\xi = Mn$ inside the free-surface Hartmann layer. Combining the stretched t-component of the momentum equation, the θ-directional component of Ohm's law and the conservation of mass yields the governing equations for the variables v_n, v_t, and j_θ of this meridional problem. The n-component of the momentum equation indicates that the pressure is continuous through the Hartmann layer. We found that the tangential velocity component is a quantity of $O(M)$ and the normal velocity component as well as the pressure terms are magnitudes of $O(1)$ through the dimensional analysis for the stretched meridional governing equations. The $O(M)$ terms of the tangential component of momentum equation and the θ-component of Ohm's law give the following differential equation for v_t:

$$\frac{\partial^2 v_t}{\partial \xi^2} - \cos^2(\lambda) v_t = 0. \tag{9a}$$

With the $O(M)$ v_t term approaching $O(1)$ velocities in the core region for the boundary condition near the core region interface, i.e.

$$v_t \to 0, \quad \text{as} \quad \xi \to -\infty \tag{9b}$$

and the resulting dimensionless boundary condition for the balance between the tangential surface tension gradient and the viscous shear stress at the free surface

$$\partial v_t/\partial \xi = -M \partial T/\partial t, \quad \text{at} \quad \xi = 0. \tag{9c}$$

The solution to (9a)–(9c) is

$$v_t = -\frac{M}{\cos(\lambda)} \frac{\partial T(0,t)}{\partial t} \exp(\cos(\lambda)\xi). \tag{10a}$$

From continuity inside the free-surface Hartmann layer, we obtain the normal velocity component, v_n

$$v_n = \frac{1}{r}\frac{\partial}{\partial t}\left\{\frac{r}{\cos^2(\lambda)}\frac{\partial T(0,t)}{\partial t}[\exp(\cos(\lambda)\xi) - 1]\right\}. \tag{10b}$$

Through Ohm's law, the azimuthal electric current density j_θ is also derived with v_t and v_n giving

$$j_\theta = -M\frac{\partial T(0,t)}{\partial t}\exp(\cos(\lambda)\xi). \tag{10c}$$

Second, we treat the lower outer core region. From the momentum equation, the z-component reveals that the core pressure is independent of z. The r-component then indicates that the core radial velocity is also independent of z. From the conservation of mass, the net flux, driven by the thermocapillarity, across any constant r-cylinder in the melt through the core region and the free-surface Hartmann layer is zero. The flow rate Q_f inside the free-surface Hartmann layer is integrated

$$Q_f = \frac{2\pi r}{\cos\lambda}\int_{HL} v_t \, dn = \frac{2\pi r}{\cos^2\lambda}\frac{\partial T(0,t)}{\partial t} \tag{11a}$$

where HL represents the Hartmann layer.

The total flow rate inside the lower outer core region, Q_l, is

$$Q_l = -Q_f = 2\pi r[g_2(r)+1]v_{rl}(r). \tag{11b}$$

Therefore, the r-directional velocity component in the core region is derived from equations (11)

$$v_{rl} = -\frac{\partial T(0,t)}{\partial t}\Big/[\cos^2(\lambda)(g_2(r)+1)]. \tag{12a}$$

Ohm's law and the z-component of the momentum equation yield the following identity:

$$v_{rl} = -j_{\theta l} = -dp_l(r)/dr \tag{12b,c}$$

from the continuity equation

$$v_{zl} = \frac{1}{r}\frac{d}{dr}\left(r\frac{dp_l}{dr}\right)[z+1] \tag{12d}$$

implying

$$\frac{dp_l(r)}{dr} = [(1+g_2'^2(r))/(g_2(r)+1)]\frac{\partial T(0,t)}{\partial t}.$$

The stream function ψ_l for the flow in the core zone of the melt

$$\psi_l = -r(z+1)\frac{dp_l}{dr} \tag{13}$$

is obtained from v_{rl} and v_{zl}. The corresponding equations for the upper outer core region are obtained by replacing (g_2+1) by $(1-g_1)$ and $(z+1)$ by $(1-z)$.

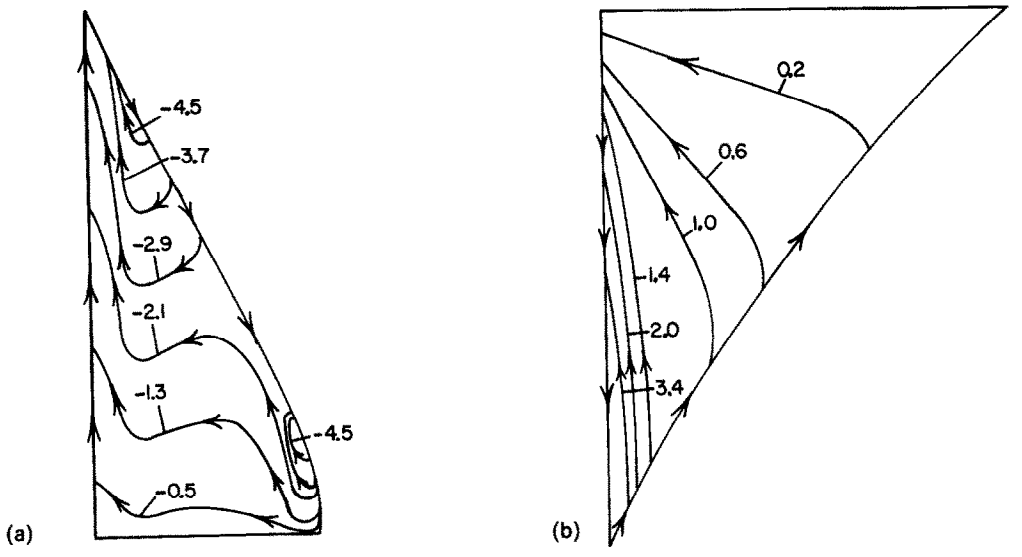

FIG. 8. The streamlines, nondimensionalized by v_{th}, due to thermocapillarity in the melt for (a) the lower outer core region and (b) the upper outer core region.

Figure 8(a) shows the streamlines in the lower core region.

For the completeness of the melt flow, we must examine the interaction region near the free surface at the melt–crystal interface edge and the free shear layer which separates the inner and outer core regions. This interaction region at the melt–crystal edge is called the singularity of Hartmann layer, for $\cos\lambda \to 0$, by Roberts [13]. This complicated Hartmann layer singularity has the dimension of $O(M^{-2/3})$ thickness and $O(M^{-1/3})$ height along the surface (see ref. [13]). From the tangential velocity component of the free-surface layer, equation (10a), this singular phenomenon is verified. The streamlines, calculated from equation (13), at the lower right corner of the outer core region also reveal this phenomenon. The flow enters this interaction region from the free-surface Hartmann layer and leaves to the lower outer core region. There is a strong local circulation through the free-surface layer, intersection region and outer core because $\cos\lambda$ is locally small (see Fig. 8(a)).

The governing equation for the free shear layer is derived from the meridional components of the momentum equation and the continuity equation, while the boundary conditions for this region arise from matching the corresponding flow variables in the core regions. Here we treat the free shear layer stream function ψ_f, governed by

$$\frac{\partial^2\psi_f}{\partial z_1^2} = \frac{\partial^4\psi_f}{\partial R^4}, \quad \text{for} \quad 0 \leqslant z_1 \leqslant g_2(a)+1 \quad \text{and} \quad -\infty \leqslant R \leqslant \infty$$

$$\psi_f = 0, \quad \text{at} \quad z_1 = 0, \quad \text{and at} \quad z_1 = g_2+1$$

$$\psi_f = 0, \quad \text{as} \quad R \to -\infty$$

$$\psi_f \to -a(z+1)\frac{dp_1(a)}{dr}, \quad \text{as} \quad R \to \infty$$

where $z_1 = z+1$, $R = M^{1/2}(r-a)$, and $r = a$ is the minimum radius (see Fig. 2). This boundary value problem can be solved with Fourier series in variable y [8] although we do not present the solutions here. The solutions indicate that the free shear layer completes the circulation path between the free-surface layer as it approaches the neck at $r = a$ and the uniform radial flow in the lower outer core at $r = a$.

The melt–crystal interface Hartmann layer is a rather passive region which does not affect the main circulation in the lower outer core region. With the no-slip boundary condition applied at the solidifying surface, the radially inward velocity is exponentially decaying from the interface at the inviscid outer core region to the solidifying interface.

The solutions for the upper core region and its adjacent regions are obtained by repeating the same procedures as in the lower region. The non-uniform temperature distribution along the free surface of the upper half melt drives the shear stress which causes the circulation in these upper regions. The stream function ψ and the radial pressure gradient p_{uc} for the upper outer core region are given as

$$\psi = -r(1-z)\frac{dp_{uc}}{dr}$$

$$\frac{dp_{uc}}{dr} = [(1+g_1'^2)/(1-g_1)]\frac{\partial T(0,t)}{\partial t}.$$

Figure 8(b) shows the streamlines in this upper half region. Notice that the temperature distribution along the free surface of the upper half melt is decreasing monotonically with increasing t. This result is in contrast to the corresponding one in the lower half melt, where the streamlines contain a small portion of up-flowing stream due to the sign changes of the tangential temperature gradient along the free surface

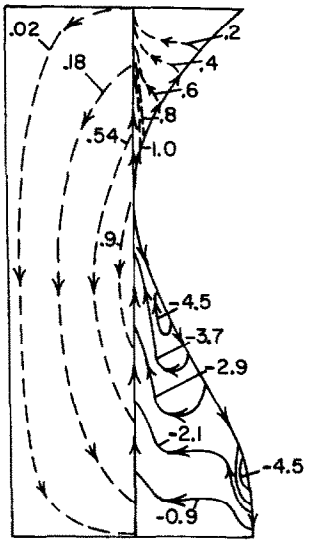

FIG. 9. The streamlines, nondimensionalized by v_{th}, for the thermal convective motion with the buoyancy and the thermocapillary effects combined.

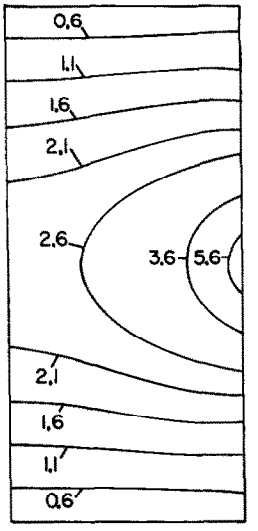

FIG. 10. The isotherms for a simplified cylindrical melt with $Pe = 0$, $\varepsilon_m = 0.8$, and $T_e = 1660$ K.

near the induction coil. Notice that the direction of all the circulations in the upper half region is counterclockwise.

4. COMBINED MOTION OF BUOYANCY AND THERMOCAPILLARITY

According to Tables 1 and 2, the magnitudes of the interaction numbers N of the buoyancy driven flow and the thermocapillary flow imply that the error (N^{-1}) of neglecting the inertial effect is much smaller than the error $(\alpha\Delta T)$ of the Boussinesq assumption of constant physical properties for $B > 0.3$ T. Also the Peclet numbers of both cases are quite small, especially for the thermocapillary flow, when the axial magnetic field strength is greater than 0.3 T. Therefore, the circulations from buoyancy and thermocapillarity can be superimposed to form the resulting thermal motion under the assumption of a strong axial magnetic field. The dimensionless magnitudes of stream functions for both cases are adjusted, according to the ratio (18.1122) of the characteristic velocities v_b to v_{th}, and added together in the outer core regions. Figure 9 shows the combined circulation of buoyancy and thermocapillarity. The magnitudes of the stream functions in Fig. 9 are nondimensionalized by v_{th}.

In the inner core region, the buoyancy driven flow is not affected by the surface tension driven flow. The reason is that the thermocapillarity flow, which is damped in the free shear layer by the strong axial magnetic field, is not able to penetrate through the free shear layer into the inner core region. As to the two outer core regions, the motion is dominated by the thermocapillarity effect. In the lower outer core region, the thermocapillary flow is slightly accelerated by the buoyancy driven flow. While in the upper outer core region, the thermocapillary flow is opposed by the opposite buoyancy driven flow. But the flow in this upper core region is still controlled by thermocapillarity.

The up-flowing jet inside the free shear layer for the combined motion is different from the buoyancy-driven jet in the free shear layer. For the free shear layer of the lower half melt, $z \leqslant 0$, both the inner core and the lower outer core circulations enter the free shear layer to form the up-flowing stream. At $z = 0$, part of the up-flowing stream will return to the free-surface Hartmann layer of the lower outer core region due to the negative tangential surface temperature gradient. This downward surface-layer flow is the incoming flow of the lower outer core region. When the up-flowing stream enters the free shear layer of the upper half melt, i.e. $z \geqslant 0$, it turns into three branches. One enters the free-surface Hartmann layer of the upper outer core region. Another enters the inner core region. The rest keeps flowing up, gathering flow from the upper outer core region and releasing flow into the inner core region simultaneously. In Fig. 9, darker lines indicate stronger circulation and dashed lines represent weaker circulation. Note that the magnitude of the radial velocity at the crystal–melt interface of the lower outer core region is about 11 times faster than that of the inner core region, as estimated from the dimensionless stream functions in Fig. 9.

5. DISCUSSION

The isotherms for a simplified cylindrical melt shape were obtained analytically. These isotherms, shown in Fig. 10, are similar to the isotherms obtained numerically by Chang and Wilcox [7], for small Peclet number. The isotherms for the hour-glass shaped melt, Fig. 5, still have the same trend as in the cylindrical shaped melt. However, the streamlines for these two different geometries are dramatically differ-

ent. With the cylindrical shape considered, there are no effects of the curvature of the free surface, so that the flow driven by the thermocapillary effect in the cylindrical melt is not so complex as the flow in the hour-glass shaped melt.

For the assumed values of the electromagnetic Bond number $\varepsilon_m = 0.8$ and the axial magnetic field strength $B = 0.5$ T, the maximum velocity ($\simeq 0.151$ mm s^{-1}), calculated from the magnitudes of ψ for the combined flow, occurs at the dimensionless location (0.61, −0.15) which is very close to the hottest point in the melt. For a moderate crystal growth rate, e.g. a crystal-pulling speed of 5 cm h^{-1}, the maximum velocity ($\simeq 54$ cm h^{-1}) is much faster than the crystal growth velocity. Therefore, the crystal growth speed is negligible. Note that both characteristic velocities, v_b and v_{th}, are proportional to B^{-2}, so that the maximum velocity will be significantly increased as the axial magnetic field strength decreased. For example, decreasing the axial magnetic field strength from 0.5 to 0.4 T will increase the maximum velocity from 54 to 84 cm h^{-1}, while further decrease in the axial magnetic field strength will violate our basic assumption for neglecting the convective effect. As a result, the thermo-convective motion must be taken into account for smaller B.

We have used a thermal gradient of the surface tension, $d\gamma/dT^* = -2.79E-04$ N m^{-1} K^{-1}, corresponding to high purity of silicon. This is appropriate for the float zone process where levels of impurities and dopants are only a few parts per billion or less.

If the polycrystalline is impurity rich, then a high contamination concentration is expected in the molten silicon, so that the thermal gradient of surface tension of silicon is smaller with more impurity. Therefore, the magnitude of the thermocapillary velocity of thermocapillarity is decreased and becomes more comparable to the buoyancy velocity in the outer core regions. For example, if we consider a high oxygen concentration case with $d\gamma/dT^* = -1.043E-04$ N m^{-1} K^{-1} (after Langlois [14]), the new ratio of v_b to v_{th} will be 48.4427 which is more than twice the ratio used for Fig. 9. So that the up-flowing stream inside the free shear layer, especially the upper half part, is going to be affected by the high oxygen concentration. First, in the lower half melt, the up-flowing jet in the free shear layer gets more contribution from the buoyancy driven flow from both inner and lower outer core regions. Second, in the upper half melt, most of the up-flowing stream will enter the inner core region and less flow enters the free-surface Hartmann layer, due to the enhanced buoyancy effect in the upper outer core region. Certain impurities, such as phosphorus, evaporate from the free surface of the melt under certain conditions with the float zone process. The balance between buoyancy and thermocapillarity strongly affects the fraction of the flow actually entering the free-surface Hartmann layer. The diffusion constant for phosphorus in silicon is so small that only the fluid entering the free-surface layer can lose phosphorus by evaporation.

Figures, by Robertson and O'Connor [2], showing the spreading electrical resistance across the diameter of a crystal grown under a strong axial magnetic field, 5000 Gauss, indicate a factor of 2.5 decrease in the dopant, gallium (Ga), concentration from the inner core region to the outer core region. Gallium has a very low segregation coefficient, so it is rejected at the crystal face and builds up in the diffusion layer at the crystal face. In the present solution, there is a strong radially inward flow in the outer lower core at the crystal face. This flow would carry away much of the gallium rejected here. This flow enters the vertical free shear layer where it can pass some of its high concentration to the flow from the inner core by diffusion or mixing. There is a much weaker radial outer flow near the crystal face in the inner core so this flow picks up much less of the gallium rejected here, and thus enters the free shear layer with a lower concentration. Therefore, there is a net transfer of gallium from the outer lower core to the inner core.

Acknowledgement—This research was supported by the National Science Foundation under Grant CBT-8519976. Dr Glenn D. Robertson, Jr. of Highes Research Laboratory provided valuable information.

REFERENCES

1. D. N. Riahi and J. S. Walker, Float zone shape and stability with the electromagnetic body force due to the radio-frequency induction coil, *J. Crystal Growth* **94**, 635–642 (1989).
2. G. D. Robertson, Jr. and D. T. O'Connor, Magnetic field effects on float-zone Si crystal growth—II. Strong axial fields, *J. Crystal Growth* **76**, 111–122 (1986).
3. A. Mühlbauer, W. Erdmann and W. Keller, Electrodynamic convection in silicon floating zones, *J. Crystal Growth* **64**, 529–545 (1983).
4. K. P. Gupta, R. O. Gregory and M. Rossnick, Limitations in using kilohertz radio frequencies for float zone silicon crystals, *J. Crystal Growth* **44**, 526–532 (1978).
5. W. E. Langlois, L. N. Hjellming and J. S. Walker, Effects of the finite electrical conductivity of the crystal on hydromagnetic Czochralski flow, *J. Crystal Growth* **83**, 51–61 (1987).
6. K. H. Lie, J. S. Walker and D. N. Riahi, Centrifugal pumping in a liquid cylinder in an axial magnetic field, with application to semiconductor crystal growth, *AIAA First Nat. Fluid Dynamics Congress*, Vol. 3, pp. 2141–2147 (1988).
7. C. E. Chang and W. R. Wilcox, Analysis of surface tension driven flow in floating zone melting, *Int. J. Heat Mass Transfer* **19**, 355–366 (1976).
8. K. H. Lie, J. S. Walker and D. N. Riahi, Centrifugal pumping in the float-zone growth of silicon crystal with an axial magnetic field, *PhysicoChem. Hydrodyn.* **10**(4), 441–460 (1988).
9. J. C. Petrykowski and J. S. Walker, Liquid-metal flow in a rectangular duct with a strong non-uniform magnetic field, *J. Fluid Mech.* **139**, 302–324 (1984).
10. L. N. Hjellming and J. S. Walker, Melt motion in a Czochralski crystal puller with an axial magnetic field: uncertainty in the thermal constants, *J. Crystal Growth* **87**, 18–32 (1988).

11. L. N. Hjellming and J. S. Walker, Melt motion in Czochralski crystal puller in an axial magnetic field: motion due to buoyancy and thermocapillarity, *J. Fluid Mech.* **182,** 335–368 (1987).
12. M. Faghri, E. M. Sparrow and A. T. Prata, Finite-difference solutions of convection–diffusion problems in irregular domains, using a nonorthogonal coordinate transformation, *Numer. Heat Transfer* **7,** 183–209 (1984).
13. P. H. Roberts, Singularities of Hartmann layers, *Proc. R. Soc. London Ser. A* **300,** 94–107 (1967).
14. W. E. Langlois, A parameter sensitivity study for Czochralski bulk flow of silicon, *J. Crystal Growth* **56,** 15–19 (1982).

ECOULEMENTS AVEC FORCE DE FLOTTEMENT ET TENSION INTERFACIALE DANS LA ZONE DE CROISSANCE CRISTALLINE AVEC UN GRAND CHAMP MAGNETIQUE AXIAL

Résumé—L'écoulement piloté par le flottement dû à un gradient de température dans un bain et l'écoulement piloté par la tension interfaciale dû à une distribution non uniforme de température le long de la surface libre de la zone sont étudiés en présence d'un grand champ magnétique axial. La forme non cylindrique de la zone a un effet important sur le mouvement du bain. Les résultats montrent les régions proches de la surface libre sont contrôlées principalement par la thermocapillarité, tandis que la région interne est dominée par la force de flottement. Quelques implications pour le transfert des dopants dans la zone fondue sont discutées.

AUFTRIEBS- UND OBERFLÄCHENSPANNUNGSGETRIEBENE STRÖMUNGEN IN DER FLIESSZONE BEIM KRISTALLWACHSTUM IN ANWESENHEIT EINES STARKEN AXIALEN MAGNETFELDES

Zusammenfassung—Die thermische Auftriebsströmung in der Schmelze einer Fließzone und die oberflächenspannungsgetriebene Strömung aufgrund ungleichmäßiger Temperaturverteilung an der freien Oberfläche wird unter dem Einfluß eines starken axialen Magnetfeldes untersucht. Die nicht-zylindrische Form der Zone hat grundlegende Auswirkungen auf die Bewegungen in der Schmelze. Die Ergebnisse zeigen, daß die Gebiete nahe der freien Oberfläche vorwiegend durch die thermische Kapillarwirkung beeinflußt werden, während die Gebiete im Innern von der Auftriebsströmung dominiert sind. Die Auswirkungen auf den Stofftransport von Additiven in der geschmolzenen Fließzone werden betrachtet.

ТЕЧЕНИЯ, ВЫЗВАННЫЕ ПОДЪЕМНОЙ СИЛОЙ И ПОВЕРХНОСТНЫМ НАТЯЖЕНИЕМ, ПРИ РОСТЕ КРИСТАЛЛОВ В ЗОНЕ ВСПЛЫТИЯ В СИЛЬНОМ АКСИАЛЬНОМ МАГНИТНОМ ПОЛЕ

Аннотация—В сильном аксиальном магнитном поле исследуются свободноконвективное течение, обусловленное температурным градиентом в зоне расплава, а также течение, вызванное поверхностным натяжением и обусловленное неоднородным распределением температур вдоль свободной поверхности зоны. Найдено, что нецилиндрическая форма зоны оказывает заметное влияние на течение. Результаты показывают, что в области у свободной поверхности наибольшее воздействие оказывает термокапиллярность, а во внутренней области—свободная конвекция. Обсуждаются некоторые выводы по массопереносу примесей в расплавленной зоне всплытия.